Pixel-based subsets for rapid multi-pinhole SPECT reconstruction

Pixel-based subsets for rapid multi-pinhole SPECT reconstruction

Woutjan Branderhorst[1,2]**, Brendan Vastenhouw**[1,2,3,4] **and Freek J Beekman**[1,2,3,4,5]

[1] Image Sciences Institute, University Medical Center Utrecht, The Netherlands
[2] Rudolf Magnus Institute of Neuroscience, University Medical Center Utrecht, The Netherlands
[3] MILabs B.V., Utrecht, The Netherlands
[4] Section Radiation, Radionuclides & Medical Imaging, Delft University of Technology, Delft, The Netherlands

E-mail: f.j.beekman@tudelft.nl

Abstract

Block-iterative image reconstruction methods, such as ordered subset expectation maximization (OSEM), are commonly used to accelerate image reconstruction. In OSEM, the speed-up factor over maximum likelihood expectation maximization (MLEM) is approximately equal to the number of subsets in which the projection data are divided. Traditionally, each subset consists of a couple of projection views, and the more subsets are used, the more the solution deviates from MLEM solutions. We found for multi-pinhole single photon emission computed tomography (SPECT) that even moderate acceleration factors in OSEM lead to inaccurate reconstructions. Therefore, we introduce pixel-based ordered subset expectation maximization (POSEM), which is based on an alternative subset choice. Pixels in each subset are spread out regularly over projections and are spatially separated as much as possible. We validated POSEM for data acquired with a focusing multi-pinhole SPECT system. Performance was compared with traditional OSEM and MLEM for a rat total body bone scan, a gated mouse myocardial perfusion scan and a Defrise phantom scan. We found that POSEM can be operated at acceleration factors that are often an order of magnitude higher than in traditional OSEM.

(Some figures in this article are in colour only in the electronic version)

1. Introduction

In recent years, statistical iterative algorithms have become the method of choice for reconstructing single photon emission computed tomography (SPECT) and positron emission

---

[5] Author to whom any correspondence should be addressed.

tomography (PET) images (Hutton *et al* 1997, Leahy and Byrne 2000, Leahy and Qi 2000, Beekman *et al* 2002, Qi and Leahy 2006), while they also receive strong interest for reconstruction of x-ray computed tomography (CT) images (Manglos *et al* 1995, Nuyts *et al* 1998, Erdogan and Fessler 1999, Beekman and Kamphuis 2001, De Man *et al* 2001, Kole and Beekman 2005, Zbijewski and Beekman 2006, Zbijewski *et al* 2007). Compared to analytic methods of reconstruction, iterative methods have been shown to be more robust to statistical noise and allow better modeling of the physical detection process, which can be used to correct for several image-degrading effects. Of these iterative methods, maximum-likelihood expectation maximization (MLEM) (Shepp and Vardi 1982) has become the gold standard, mostly due to its consistent and predictable convergence behavior, non-negativity constraints and ease of implementation. A major drawback of MLEM is that it is computationally very costly. In addition to the introduction of faster computers, a major breakthrough that led to its widespread application in medical image reconstruction was the introduction of block-iterative methods like ordered subset expectation maximization (OSEM) (Hudson and Larkin 1994). A primer to principles and clinical applications of ordered subset reconstruction can be found in Hutton *et al* (1997).

Empiric studies have shown that for many SPECT collimation geometries, OSEM provides almost the same reconstructed images as MLEM, when the acceleration is not pushed too much (Kamphuis *et al* 1996, Lalush and Tsui 2000). The acceleration factor of OSEM is roughly proportional to the number of subsets used (Hudson and Larkin 1994, Kamphuis *et al* 1996). In most implementations, each subset contains a number of complete SPECT projections. Traditionally, the acceleration factor is increased by lowering the number of projections per subset, but this can have adverse effects on reconstructed image noise and quantitative accuracy if too few projections are used per subset.

To our knowledge, only little has been published on block-iterative methods in which subsets do not each consist of a number of complete SPECT projections. In the context of list-mode block-iterative image reconstruction for PET, Levkovitz *et al* (2001) proposed their COSEM algorithm. In this algorithm, subsets are chosen by combining list-mode events acquired during a certain time interval, at certain angles, or completely random. However, the study did not elaborate on the effect of the various subset choices. Kadrmas (2001) reported interesting results using dynamic subsets based on the distribution of tomographic and statistical information in the measured data. For dynamic studies, Rahmim *et al* (2005) proposed to anticipate the changes in activity distribution over time by dividing time intervals into portions and assigning one portion from each time interval to each subset.

To obtain OSEM solutions that are close to MLEM images, it is important to preserve subset balance, which according to Hudson and Larkin (1994) means that voxel activity contributes about equally to all subsets. The issue of subset choice turns out to be of particular concern in multi-pinhole SPECT systems (e.g. Beekman and Vastenhouw (2004), Furenlid *et al* (2004), Beekman *et al* (2005), Van der Have *et al* (2009)). For these systems, OSEM images exhibit artifacts already at a low number of subsets, as we will show in the next sections. The most important reason may be that subset balance is very difficult to achieve in complex pinhole geometries with inherently voxel-position-dependent sensitivities, a different number of pixels per projection and truncated projections. The goal of this paper is to propose and experimentally validate a new subset choice ('pixel-based subsets') which is easy to implement and enables very high acceleration factors, even on stationary focusing multi-pinhole SPECT systems with complex pinhole geometries and severely truncated projection views.

2. Methods

We implemented and validated our method on a U-SPECT-II system (Van der Have *et al* 2009) (MILabs, Utrecht, The Netherlands), an ultra-high-resolution focusing multi-pinhole SPECT system for small animals. This section first introduces the pinhole geometry of U-SPECT-II. Next, a description of the implementation of the traditional ordered subset algorithm and the pixel-based ordered subset expectation maximization (POSEM) for U-SPECT-II is given. Finally, we describe how POSEM was validated.

2.1. Focusing multi-pinhole SPECT scanner

U-SPECT-II employs exchangeable cylindrical collimators containing 75 pinholes that can be mounted in the center of three stationary NaI gamma cameras that are placed in a triangle. Without moving any parts of the scanner, this setup allows collecting complete data from the central field-of-view (CFOV), which is the area that is observed by all pinholes simultaneously. Optical photos are acquired by three webcams for volume of interest selection before SPECT acquisition. Data are acquired in list-mode format, which stores position, energy and detection time for each scintillation on the detector. With an XYZ translation stage, an animal can be moved inside the collimator during imaging. This can be used for optimal imaging of objects larger than the CFOV. Using this dedicated acquisition method, called the scanning focus method (SFM) (Vastenhouw and Beekman 2007), the pinholes can collect gamma photons from different parts of the object. The SFM only leads to good images when a reconstruction algorithm is used that simultaneously uses projection data from all bed positions to reconstruct the entire volume (Vastenhouw and Beekman 2007), instead of stitching separate reconstructions of sub-volumes obtained from individual focus positions.

2.2. Image reconstruction

We have implemented the MLEM algorithm according to the formulation in Shepp and Vardi (1982):

$$\tilde{\lambda}_i^{k+1} = \frac{\tilde{\lambda}_i^k}{\sum_j c_{ij}} \sum_j \frac{c_{ij} p_j}{\sum_i c_{ij} \tilde{\lambda}_i^k}$$

where $\tilde{\lambda}_i^k$ is the value of voxel i in the kth image estimate, c_{ij} represents the probability that voxel i is detected in projection bin j and p_j are the projection measurements. U-SPECT-II employs a system matrix c that is derived from a number of point-spread-function measurements and stored on a disk (Van der Have *et al* 2008).

OSEM (Hudson and Larkin 1994) is a relatively simple adaptation to MLEM. In OSEM, the projection data are typically grouped into subsets each consisting of different projection images. While iterating, each image estimate is updated after applying the MLEM algorithm on a different subset. One iteration is defined to be completed when all subsets of projections have been used. The OSEM algorithm is given by

$$\tilde{\lambda}_i^{n+1}(k) = \frac{\tilde{\lambda}_i^n(k)}{\sum_{j \in S_n} c_{ij}} \sum_{j \in S_n} \frac{c_{ij} p_j}{\sum_i c_{ij} \tilde{\lambda}_i^n(k)}$$

where $\tilde{\lambda}_i^{n+1}(k)$ represents the image update after processing subset n, S_n contains the projection angles of subset n and k represents the iteration number.

To reconstruct the data from multiple bed positions, the above-described MLEM and OSEM algorithms were adapted according to (Vastenhouw and Beekman 2007).
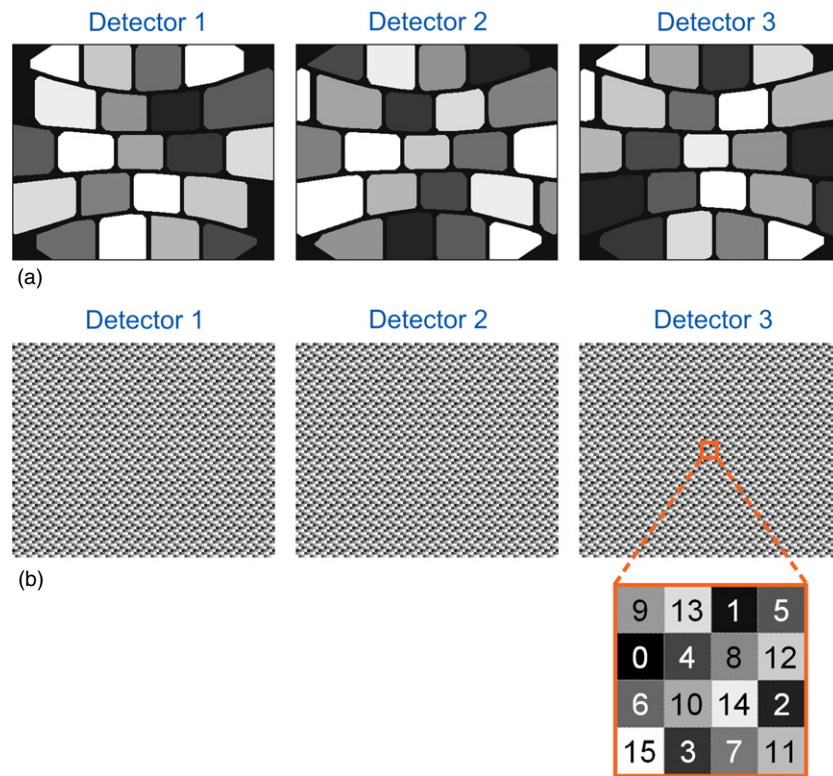
Figure 1. Example subset distributions for traditional OSEM and POSEM. Pixels having the same gray shade belong to the same subset. (a) 15 traditional OSEM subsets. (b) 16 POSEM subsets (simplified; in reality the detector contains many more pixels). A detail of the repeating pattern used to create 16 POSEM subsets is magnified.

2.3. Selection of traditional OSEM subsets

Each of the three large-field-of-view detectors of the U-SPECT-II is divided into non-overlapping pinhole projections (see figure 1(a)). To implement traditional OSEM, these complete projections were distributed over the subsets as follows. The 75 pinholes in the U-SPECT-II are located in five pinhole rings. We defined 15 subsets consisting of 5 pinhole projections, 1 from each ring. Within one subset, the projections were chosen such that the angular separation of projections from neighboring rings was as close as possible to 90°. To approximate maximal angular separation between subsequently processed subsets, the subsets were ordered using a method similar to that proposed by Li *et al* (1994). Acceleration factors higher than 15 were obtained by exploiting the fact that all scans in this study were acquired using multiple bed positions. The bed positions result in different sets of projection data, each corresponding to a different position of the CFOV within the volume to be reconstructed. Based on this correspondence, the projection data in each of the 15 subsets were further subdivided into groups. The CFOV positions corresponding to each group were distributed regularly over the volume to be scanned, and separated maximally from the positions in other groups. Defining 2, 4 and 8 groups of CFOV positions, we obtained respectively 30, 60 and 120 subsets.

2.4. Selection of subsets for POSEM

In POSEM, all detector pixels are distributed into subsets independently of the pinhole projections (figure 1(b)). Detector pixels are assigned to subsets according to a pattern which is repeated over the entire detector surface. The pattern, defined on a rectangular sub-area of the detector, bijectively maps the pixels in that area onto subsets. The number of pixels in the pattern equals the number of resulting subsets. Patterns were chosen such that subsequent subsets were well separated. As a result of this approach, the pixels in each POSEM subset are spread out regularly over the detector surface. Since a pre-computed transfer matrix is used, this choice of subsets does not influence the system response modeling and the computation time required for one iteration. Figure 1(b) displays the pattern for 16 subsets.

We used the 16-subset pattern as a building block to create patterns for higher numbers of subsets. To describe this, the patterns can be represented more conveniently as matrices in which the elements are integer numbers denoting to which subset the corresponding pixel is mapped. For example, the matrix representation of the 16-subset pattern shown in figure 1(b) is

$$P_{16} = \begin{bmatrix} 9 & 13 & 1 & 5 \\ 0 & 4 & 8 & 12 \\ 6 & 10 & 14 & 2 \\ 15 & 3 & 7 & 11 \end{bmatrix}$$

Based on P_{16}, the patterns for 32, 64 and 128 subsets were constructed as follows:

$$P_{32} = [\, 2P_{16} \quad 2P_{16} + 1 \,]$$

$$P_{64} = \begin{bmatrix} 4P_{16} & 4P_{16} + 1 \\ 4P_{16} + 2 & 4P_{16} + 3 \end{bmatrix}$$

$$P_{128} = \begin{bmatrix} 8P_{16} & 8P_{16} + 1 & 8P_{16} + 2 & 8P_{16} + 3 \\ 8P_{16} + 4 & 8P_{16} + 5 & 8P_{16} + 6 & 8P_{16} + 7 \end{bmatrix}$$

2.5. Evaluation

To test the performance of POSEM, we reconstructed rat total body bone images, mouse myocardial perfusion images and images of a Defrise phantom. Animal studies were conducted following protocols as approved by the Animal Research Committee of the University Medical Center Utrecht. In the rat bone scan, a rat was injected with [99mTc]-hydroxymethylene diphosphonate ([99mTc]-HDP). Details can be found in Van der Have *et al* (2009). For the mouse myocardial scan, a 29 g male mouse (C57BL/6JO1aHsd) was anesthetized with isoflurane anesthesia and injected with 0.3 ml [99mTc]-tetrafosmin (580 MBq). At 1 h and 30 min after radioligand injection, an acquisition of 1 h was performed using the 0.35 mm diameter pinhole mouse collimator tube (Van der Have *et al* 2009).

The Defrise phantom used in this study consists of a set of parallel polymethylmethacrylate disks. The space between the disks was filled with activity. The 20 mm diameter disks are 1.5 mm thick and the spacing between them equals their thickness. The length of the phantom is 25.5 mm. The Defrise phantom has been proven useful for investigating the effects of incomplete data that occur in cone-beam-like imaging geometries and was chosen for the present study since incompleteness of data plays a role during each OSEM sub-iteration. The phantom was filled with 306 MBq [99mTc]-pertechnetate and scanned for 30 min using the 0.6 mm diameter pinhole mouse collimator tube (Van der Have *et al* 2009).

Images were reconstructed using traditional OSEM with 15, 30, 60 and 120 subsets, and using 120 iterations MLEM (the gold standard). The number of iterations used in traditional
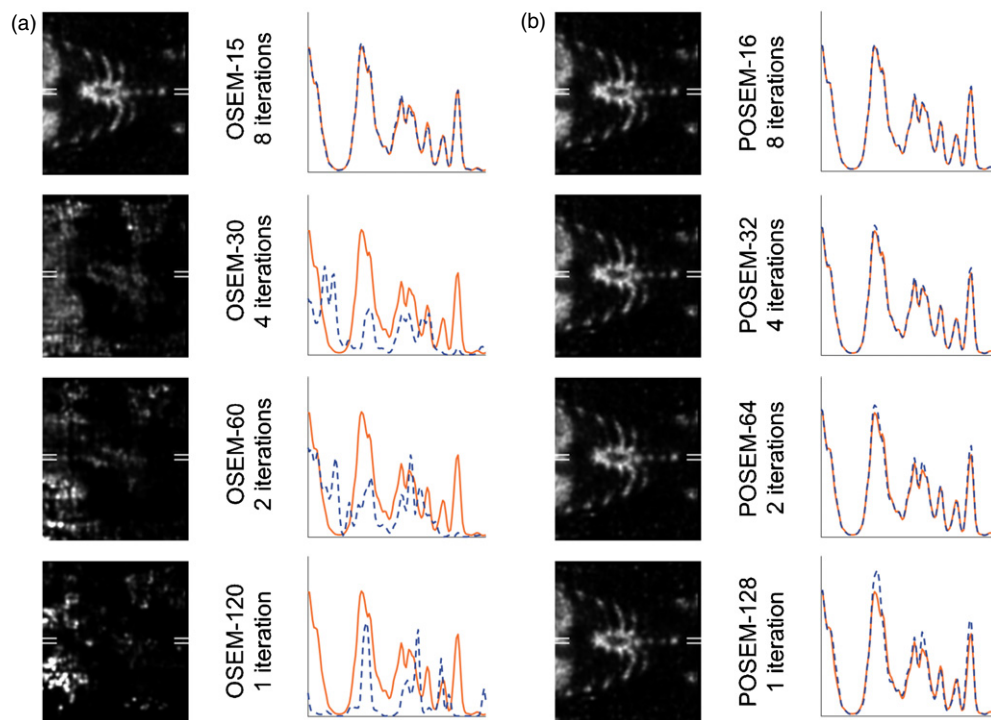
Figure 2. (a) Coronal slices and profiles from the rat bone scan, reconstructed using traditional OSEM (dashed), compared to the corresponding MLEM reconstructed image profile after 120 iterations (solid). From top to bottom: 15, 30, 60 and 120 traditional OSEM subsets. (b) The same as in (a), but for POSEM (dashed) compared to the corresponding MLEM reconstructed image profile after 128 iterations (solid). From top to bottom: 16, 32, 64 and 128 POSEM subsets.

OSEM was respectively 8, 4, 2 and 1. This is based on the rule of thumb that applying x iterations OSEM with y subsets leads to an approximately equivalent resolution and contrast as when xy iterations MLEM are applied (Hudson and Larkin 1994). POSEM reconstructions were run using 16, 32, 64 and 128 subsets with the number of iterations set to respectively 8, 4, 2 and 1. Because with POSEM it was not possible to exactly end up in the equivalent of 120 iterations, images reconstructed using 128 iterations MLEM were used as the gold standard.

Voxel grids of the rat bone scan, the mouse myocardial perfusion scan and the Defrise phantom scan were isotropic, with voxel sizes of respectively 0.375 mm, 0.125 mm and 0.1875 mm. The reconstruction of the mouse myocardial perfusion scan employed cardiac gating with eight gates.

3. Results

Figure 2 presents the traditional OSEM and POSEM reconstructed images from the rat bone scan, on which a Gaussian post-filter with sigma = 0.375 mm was applied. We extracted image profiles through the sternum from a coronal slice through the thorax. The profile width was 1.125 mm (3 voxels) and the slice thickness was 0.375 mm.

Whereas the image obtained using 15 traditional OSEM subsets still corresponds well to its MLEM equivalent, the images resulting from 30 or more traditional OSEM subsets are
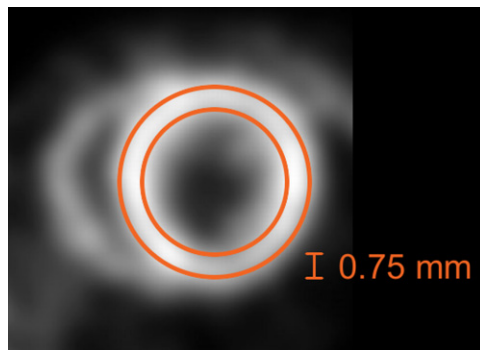
Figure 3. Short-axis image of mouse myocardium with example of the circumferential profile over the left ventricular wall.

Table 1. Mean and maximum deviations from MLEM bone scan image profiles.

Traditional OSEM			POSEM		
	Mean	Max		Mean	Max
15 subsets	1.12%	3.88%	16 subsets	0.50%	2.54%
30 subsets	23.96%	92.98%	32 subsets	1.06%	5.01%
60 subsets	19.48%	78.23%	64 subsets	1.85%	8.01%
120 subsets	24.18%	88.95%	128 subsets	3.42%	23.82%

Values are percentages of the maximum value in the profile of the MLEM image.

completely distorted by artifacts. POSEM remains very close to the MLEM image shape as the number of subsets is increased.

Table 1 quantifies the intensity deviations of the image profiles from the corresponding MLEM estimate for the rat bone scan. The intensity differences for 32 and 64 POSEM subsets are of the same order as in the case of 15 traditional OSEM subsets. Although we measured a relatively large maximum deviation in the 128-subset POSEM image, the mean deviations are almost an order of magnitude smaller than in the case of 30 traditional OSEM subsets.

Figure 4 presents the images of the myocardial perfusion scan, reconstructed using traditional OSEM and POSEM. The mouse myocardial reconstructions were post-filtered spatially using a 3D Gaussian filter with sigma = 0.3 mm and temporally using a Gaussian with sigma = 0.85 gating intervals. We generated circumferential profiles from a short-axial slice at the center of the heart by dividing the profile range (depicted in figure 3) into 18 segments and calculating, for each segment, the mean voxel value after summing the images of all gating intervals. The profile width was 0.75 mm and the slice thickness was 0.375 mm.

Already at 15 traditional OSEM subsets, the reconstructed images show significant differences in image intensity compared to the MLEM equivalent, whereas the myocardium becomes indistinguishable when using 30 or more subsets. Visually, POSEM retains almost the same image, even when 128 subsets and cardiac gating are employed. Details such as the papillary muscles and right ventricle wall remain visible in all POSEM images, although the ventricle walls appear slightly noisier in the 64- and 128-subset cases.
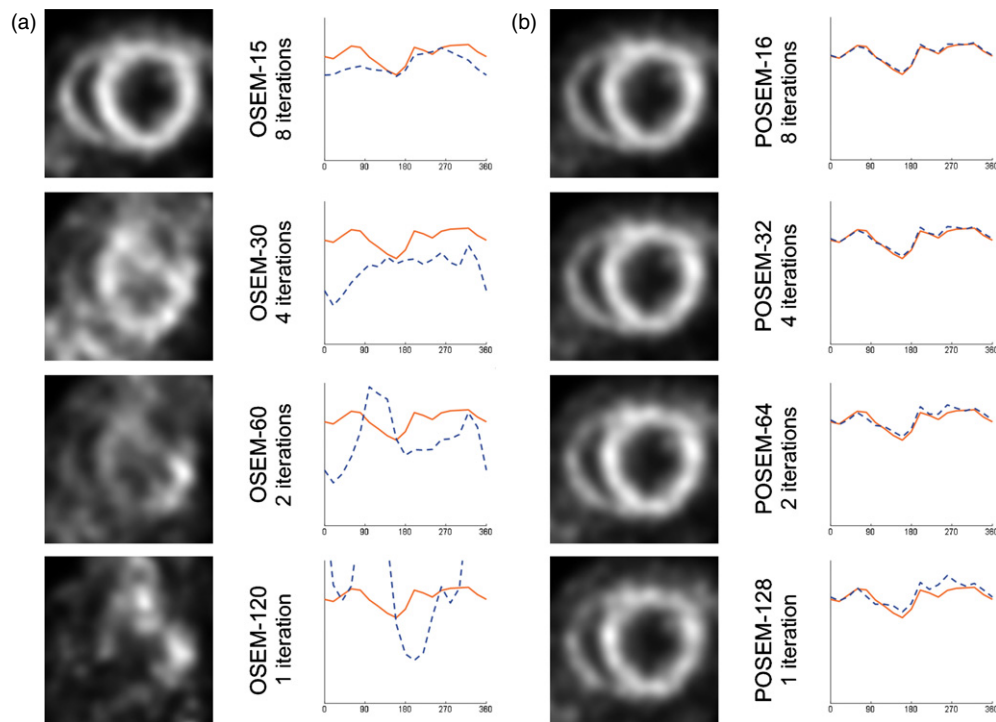
Figure 4. (a) Short-axis slices and circumferential profiles from the mouse myocardial scan, reconstructed using traditional OSEM (dashed), compared to the corresponding MLEM reconstructed image profile after 120 iterations (solid). From top to bottom: 15, 30, 60 and 120 traditional OSEM subsets. (b) The same as in (a), but for POSEM (dashed) compared to the corresponding MLEM reconstructed image profile after 128 iterations (solid). From top to bottom: 16, 32, 64 and 128 POSEM subsets.

Table 2. Mean and maximum deviations from MLEM myocardial perfusion scan image profiles and contrast between the left ventricle and left ventricular wall.

Traditional OSEM				POSEM			
	Mean	Max	Contrast		Mean	Max	Contrast
1 subset (MLEM)	0%	0%	0.7620	1 subset (MLEM)	0%	0%	0.7620
15 subsets	9.08%	18.68%	0.8050	16 subsets	1.01%	2.25%	0.7630
30 subsets	27.01%	54.57%	0.2692	32 subsets	1.57%	3.99%	0.7634
60 subsets	27.30%	50.81%	0.3333	64 subsets	2.63%	6.85%	0.7629
120 subsets	49.73%	144.55%	0.3972	128 subsets	4.29%	12.70%	0.7672

Mean and max values are percentages of the maximum value in the profile of the MLEM image.

We have quantified the deviations of the myocardial image profiles from their MLEM equivalents in table 2. Even the 128-subset POSEM reconstruction shows a smaller maximum deviation from the MLEM profile than the 15-subset traditional OSEM reconstruction. This means that a speed increase of almost an order of magnitude is possible using POSEM, compared to traditional OSEM.

In the myocardial perfusion images, contrast was calculated as $(m - c)/m$, where m equals the mean voxel value in a region-of-interest (ROI) within the left ventricular wall and c is
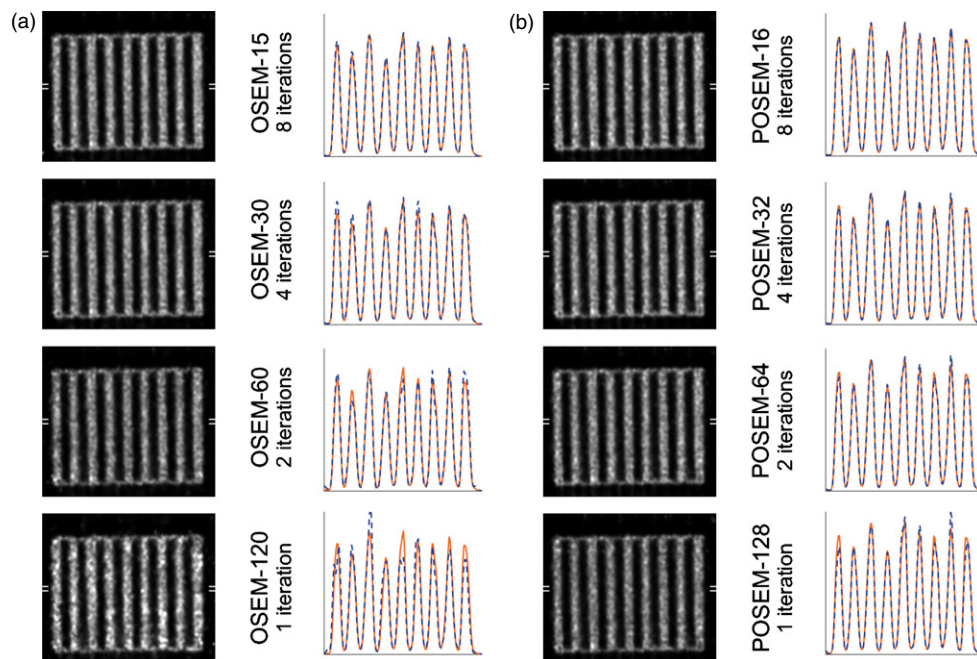
Figure 5. (a) Sagittal slices and profiles from the Defrise phantom scan, reconstructed using traditional OSEM (dashed), compared to the corresponding MLEM reconstructed image profile after 120 iterations (solid). From top to bottom: 15, 30, 60 and 120 traditional OSEM subsets. (b) The same as in (a), but for POSEM (dashed) compared to the corresponding MLEM reconstructed image profile after 128 iterations (solid). From top to bottom: 16, 32, 64 and 128 POSEM subsets.

Table 3. Mean and maximum deviations from MLEM Defrise phantom scan image profiles.

Traditional OSEM			POSEM		
	Mean	Max		Mean	Max
15 subsets	1.22%	5.32%	16 subsets	0.38%	1.93%
30 subsets	1.94%	9.97%	32 subsets	0.60%	3.91%
60 subsets	2.82%	12.04%	64 subsets	1.19%	7.64%
120 subsets	5.59%	27.02%	128 subsets	2.21%	13.34%

Values are percentages of the maximum value in the profile of the MLEM image.

the mean voxel value in a ROI within the ventricular cavity. ROI means were calculated on the summed images of all gating intervals. Opposed to traditional OSEM, POSEM maintains image contrast even with very high speed-up factors (see table 2).

Figure 5 presents the traditional OSEM and POSEM reconstructed images of the Defrise phantom after applying a Gaussian post-filter with sigma = 0.1875 mm. Longitudinal image profiles are shown from sagittal slices, perpendicular to the direction of the disks. Both the profile width and the slice thickness were 0.1875 mm. The traditional OSEM approach performs reasonably well, but for high numbers of subsets, the images are much noisier than the corresponding POSEM images and the image profiles show much larger deviations from MLEM.

Table 3 shows how much the Defrise phantom image profiles deviate in intensity from their MLEM equivalents for various numbers of subsets. The maximum deviations resulting

from 32 and 64 POSEM subsets are smaller than those resulting from respectively 15 and 30 traditional OSEM subsets. Although the maximum deviation using 128 POSEM subsets is larger than the maximum deviation obtained using 60 traditional OSEM subsets, the mean deviation is lower and the mean deviation obtained using 64 POSEM subsets is even smaller than the mean deviation using 15 traditional OSEM subsets.

4. Conclusion and discussion

This paper presents a novel method for choosing ordered subsets (POSEM), which was tested on a focusing multi-pinhole SPECT device dedicated to imaging small animals with sub-half-mm resolution. For this SPECT system employing a pre-computed transfer matrix, POSEM allows significant improvements in image reconstruction speed-up compared to traditional selection of ordered subsets. As we showed both in physical phantoms and in animal experiments, POSEM can be very valuable in pinhole SPECT imaging. When ordered subset methods are applied to truncated projections, a common problem is that some voxels are not sampled by any of the elements of a certain subset, in which case the normalization term of the update equation equals zero. This situation, in which the voxel value is left unchanged to suppress artifacts (Hudson and Larkin 1994), may occur less often in POSEM than in OSEM. This may be one of the causes that POSEM performs very well in severely truncated SPECT projections.

Several multi-pinhole SPECT devices for clinical imaging have been proposed over recent decades (e.g. Vogel *et al* (1978), Rowe *et al* (1993), Beekman and Van der Have (2007), Funk *et al* (2006), Steele *et al* (2008)). Based on initial tests on several other simulated clinical and pre-clinical pinhole SPECT systems as described in Goorden *et al* (2009) and Goorden and Beekman (2010), we believe that POSEM works well over a wide range of multi-pinhole systems. Iterative PET reconstruction may also benefit from the POSEM approach proposed in here, and further research needs to be performed to see what kind of acceleration factor can be obtained. When reconstruction algorithms are being used which calculate re-projections on-the-fly, for example such as used in 3D Monte Carlo-based reconstruction (e.g. Beekman *et al* (2002), Xiao *et al* (2006), (2007), Sohlberg *et al* (2008)) POSEM may become complicated and inefficient.

Acknowledgments

References

Beekman F and Kamphuis C 2001 Ordered subset reconstruction for x-ray CT *Phys. Med. Biol.* **46** 1835–44

Beekman F J, De Jong H W A M and Van Geloven S 2002 Efficient fully 3D iterative SPECT reconstruction with Monte Carlo-based scatter compensation *IEEE Trans. Med. Imaging* **21** 867–77

Beekman F and Van Der Have F 2007 The pinhole: gateway to ultra-high-resolution three-dimensional radionuclide imaging *Eur. J. Nucl. Med. Mol. Imaging* **34** 151–61

Beekman F J, Van Der Have F, Vastenhouw B, Van Der Linden A J, van Rijk P P, Burbach J P and Smidt M P 2005 U-SPECT-I: a novel system for submillimeter-resolution tomography with radiolabeled molecules in mice *J. Nucl. Med.* **46** 1194–200

Beekman F J and Vastenhouw B 2004 Design and simulation of a high-resolution stationary SPECT system for small animals *Phys. Med. Biol.* **49** 4579–92

De Man B, Nuyts J, Dupont P, Marchal G and Suetens P 2001 An iterative maximum-likelihood polychromatic algorithm for CT *IEEE Trans. Med. Imaging* **20** 999–1008

Erdogan H and Fessler J 1999 Ordered subsets algorithms for transmission tomography *Phys. Med. Biol.* **44** 2835–51

Funk T, Kirch D L, Koss J E, Botvinick E and Hasegawa B H 2006 A novel approach to multipinhole SPECT for myocardial perfusion imaging *J. Nucl. Med.* **47** 595–602

Furenlid L R, Wilson D W, Chen Y C, Kim H, Pietraski P J, Crawford M J and Barrett H H 2004 FastSPECT II: a second-generation high-resolution dynamic SPECT imager *IEEE Trans. Nucl. Sci.* **51** 631–5

Goorden M C and Beekman F J 2010 High-resolution tomography of positron emitters with clustered pinhole SPECT *Phys. Med. Biol.* **55** 1265–77

Goorden M C, Rentmeester M C M and Beekman F J 2009 Theoretical analysis of full-ring multi-pinhole brain SPECT *Phys. Med. Biol.* **54** 6593–610

Hudson H M and Larkin R S 1994 Accelerated image reconstruction using ordered subsets of projection data *IEEE Trans. Med. Imaging* **13** 601–9

Hutton B F, Hudson H M and Beekman F J 1997 A clinical perspective of accelerated statistical reconstruction *Eur. J. Nucl. Med. Mol. Imaging* **24** 797–808

Kadrmas D J 2001 Statistically regulated and adaptive EM reconstruction for emission computed tomography *IEEE Trans. Nucl. Sci.* **48** 790–8

Kamphuis C, Beekman F J and Viergever M A 1996 Evaluation of OSEM versus MLEM for 1D, 2D and fully 3D SPECT reconstruction *IEEE Trans. Nucl. Sci.* **43** 2018–24

Kole J S and Beekman F J 2005 Evaluation of the ordered subset convex algorithm for cone-beam CT *Phys. Med. Biol.* **50** 613–23

Lalush D S and Tsui B M W 2000 Performance of ordered-subset reconstruction algorithms under conditions of extreme attenuation and truncation in myocardial SPECT *J. Nucl. Med.* **41** 737–44

Leahy R M and Byrne C 2000 Recent developments in iterative image reconstruction for PET and SPECT *IEEE Trans. Med. Imaging* **19** 257–60

Leahy R M and Qi J Y 2000 Statistical approaches in quantitative positron emission tomography *Stat. Comput.* **10** 147–65

Levkovitz R, Falikman D, Zibulevsky M, Ben-Tal A and Nemirovski A 2001 The design and implementation of COSEM, an iterative algorithm for fully 3D listmode data *IEEE Trans. Med. Imaging* **20** 633–42

Li J, Jaszczak R J, Greer K L and Coleman R E 1994 Implementation of an accelerated iterative algorithm for cone beam SPECT *Phys. Med. Biol.* **39** 643–53

Manglos S H, Gagne G M, Krol A, Thomas F D and Narayanaswamy R 1995 Transmission maximum-likelihood reconstruction with ordered subsets for cone beam CT *Phys. Med. Biol.* **40** 1225–41

Nuyts J, De Man B D, Dupont P, Defrise M, Suetens P and Mortelmans L 1998 Iterative reconstruction for helical CT: a simulation study *Phys. Med. Biol.* **43** 729–37

Qi J and Leahy R M 2006 Iterative reconstruction techniques in emission computed tomography *Phys. Med. Biol.* **51** R541–78

Rahmim A, Cheng J-C, Blinder S, Camborde M-L and Sossi V 2005 Statistical dynamic image reconstruction in state-of-the-art high-resolution PET *Phys. Med. Biol.* **50** 4887–912

Rowe R K, Aarsvold J N, Barrett H H, Chen J C, Klein W P, Moore B A, Pang I W, Patton D D and White T A 1993 A stationary hemispherical SPECT imager for three-dimensional brain imaging *J. Nucl. Med.* **34** 474–80

Shepp L A and Vardi Y 1982 Maximum likelihood reconstruction for emission tomography *IEEE Trans. Med. Imaging* **1** 113–22

Steele P P, Kirch D L and Koss J E 2008 Comparison of simultaneous dual-isotope multipinhole SPECT with rotational SPECT in a group of patients with coronary artery disease *J. Nucl. Med.* **49** 1080–9

Sohlberg A, Watabe H and Iida H 2008 Acceleration of Monte Carlo-based scatter compensation for cardiac SPECT *Phys. Med. Biol.* **53** N277–85

Van Der Have F, Vastenhouw B, Ramakers R M, Branderhorst W, Krah J O, Ji C, Staelens S G and Beekman F J 2009 U-SPECT-II: an ultra-high-resolution device for molecular small-animal imaging *J. Nucl. Med.* **50** 599–605

Van Der Have F, Vastenhouw B, Rentmeester M C M and Beekman F J 2008 System calibration and statistical image reconstruction for ultra-high resolution stationary pinhole SPECT *IEEE Trans. Med. Imaging* **27** 960–71

Vastenhouw B and Beekman F J 2007 Submillimeter total-body murine imaging with U-SPECT-I *J. Nucl. Med.* **48** 487–93

Vogel R A, Kirch D, LeFree M and Steele P 1978 A new method of multiplanar emission tomography using a seven pinhole collimator and an anger scintillation camera *J. Nucl. Med.* **19** 648–54

Xiao J, De Wit T C, Staelens S G and Beekman F J 2006 Evaluation of 3D Monte-Carlo based scatter correction for Tc-99 m cardiac perfusion SPECT *J. Nucl. Med.* **47** 1662–9

Xiao J, De Wit T C, Zbijewski W, Staelens S and Beekman F J 2007 Evaluation of 3D Monte Carlo-based scatter correction for Tl-201 cardiac perfusion SPECT *J. Nucl. Med.* **48** 637–44

Zbijewski W and Beekman F J 2006 Efficient Monte Carlo based scatter artifact reduction in cone-beam micro-CT *IEEE Trans. Med. Imaging* **25** 817–27

Zbijewski W, Defrise M, Viergever M A and Beekman F J 2007 Statistical reconstruction for x-ray CT systems with non-continuous detectors *Phys. Med. Biol.* **52** 403–41